UNIVERSITY OF CALIFORNIA,
IRVINE

Multirange Navigation on Spine Surgical Robots

THESIS

submitted in partial satisfaction of the requirements
for the degree of

MASTER OF SCIENCE

in Engineering

by

Sylwia Galka

Thesis Committee:
Assistant Professor Camilo Velez Cuervo, Chair
Distinguished Professor J. Michael McCarthy
Adjunct Professor Lawrence Kulinsky

2025

TABLE OF CONTENTS

LIST OF FIGURES

LIST OF TABLES

ACKNOWLEDGMENTS

I would like to acknowledge my advisor, Professor Camilo Velez Cuervo, for his guidance, support, and expertise throughout my research. His insights and encouragement have been invaluable, and I deeply appreciate that. His support has played a significant role in shaping my academic journey and making this achievement possible. Through this work, I have gained knowledge in a field that was entirely new to me, and this learning experience has been both challenging and rewarding.

I am also grateful to the members of my thesis committee, Professor J. Michael McCarthy and Professor Lawrence Kulinsky, for their time, expertise, and commitment to this process. Their support and valuable insights are deeply appreciated.

Additionally, I would like to thank my fellow lab members (Magnetic Microsystems & Microrobotics lab) for their support and technical assistance and for creating a supportive research environment. Their willingness to share knowledge and readiness to help made my research enjoyable. I would like to thank Mahtab and Naji for providing essential guidance on laboratory equipment, helping me navigate my initial steps in the lab, and offering valuable assistance with measurements. I thank Mark for designing and implementing the CNC machine setup, which enabled my measurements.

ABSTRACT OF THE THESIS

Multirange Navigation on Spine Surgical Robots

by

Sylwia Galka

Master of Science in Engineering

University of California, Irvine, 2025

Assistant Professor Camilo Velez Cuervo, Chair

Robotic surgical systems are increasingly used in spine surgery to improve accuracy and reduce radiation exposure. Accurate positioning is crucial for patient safety and successful surgical outcomes. Despite advances in robotic navigation, improving the accuracy and reliability of positioning systems remains a key focus in spinal surgery.

The thesis presents the concept of multirange hybrid navigation, which combines 1) ultra-wideband (UWB) positioning for long and medium range and 2) magnetic sensing system for short range real-time navigation in robotic-assisted spine surgery. This study will focus on presenting a proof of concept and comparing the accuracy in determining position and orientation for both techniques. This work has constrained the navigation in 2 axes (2D) as a fundamental step towards full 3D navigation.

The UWB positioning system utilizes four microcontrollers with ultra-wideband transceivers used in the configuration of 3 anchors (beacons) and one tag (conceptually integrated into a robotic arm). The system calculates distances using time-based

measurements to determine the tag's position. The UWB system was tested experimentally in 2D, in two different setups. The UWB positioning accuracy was determined by comparing actual and measured coordinates and calculating the root mean square error (RMSE) for the x and y axes. Results showed that UWB positioning was more accurate along the y-axis than the x-axis. The average value for the x and y-axes of RMSE based on both setups was 4.9 ± 3.0 cm.

The magnetic sensing system was evaluated using software-based modeling for position and orientation predictions. The system was designed to detect the angle of the magnet and the distance from the center of the magnet based on the magnetic field values B_x, B_y, and B_z read from the simulated Hall sensor. A 3D magnetic field model was generated using Magpylib, simulating field variations at different distances and angles. Machine learning (ML) models, trained on synthetic magnetic field data, predicted the orientation of the magnet and the distance to the magnet. For the single-sensor approach, the mean absolute error (MAE) of angle prediction was 10.41°. For the distance predictions, the average prediction error was 240 μm. For the two-sensors approach, the angle MAE had a value of 5.15° and a distance of 10 μm.

The findings of this study highlight the potential of integrating UWB and magnetic navigation for improved surgical guidance for spine robots. Each system plays an important role in this hybrid navigation system, and they work complementarily. The UWB positioning system is well-suited for long-range localization, providing global reference to guide the robotic arm toward the operating area. The magnetic sensing system excels in short-range, high-precision measurements necessary for precise surgical tasks such as pedicle screw placement. Future work is necessary to develop improved models for 3D applications, incorporate sensors into robotic arm, and evaluate the performance of combined sensors.

1. Introduction

Robotic surgical systems, used across various medical disciplines, have emerged as effective tools for precision procedures like spinal screw placement. Due to the high accuracy of pedicle screw placement (95-100%), this technology has led to the growth of the market. Robot-assisted surgeries, compared to fluoroscopic-assisted techniques, reduce radiation exposure for patients and surgeons, especially in mini-invasive surgery (MIS) of the spine [1].

The use of robots in minimally invasive spine procedures is increasing since MIS requires small incisions and lack of cutting muscles, compared to open spine surgery. This benefits patients, resulting in lower blood loss, less postoperative pain, and faster recovery [2]. The concept of minimally invasive surgery was born in 1987 with the first laparoscopic cholecystectomy, revolutionizing surgical approaches across different disciplines. Robotics took longer to be adopted in medicine than in other industries. In 2004, the SpineAssist (Mazor Robotics Ltd., Caesarea, Israel) became the first spine-specific surgical robot to receive FDA approval, marking an important step for robotic assistance in spinal surgeries. The robotic approach is beneficial not only for patients but also for surgeons. It eliminates hand tremors, reduces fatigue, and provides up to 7 degrees of freedom during surgery [3].

According to the iData research report in 2023, the US surgical navigation and robotics market was worth about $7 billion. The market is expected to grow 15.4% annually, reaching $18.9 billion by 2030. In the surgical robotics market, Intuitive Surgical leads with its da Vinci platforms used in general surgery. PROCEPT BioRobotics follows with its AquaBeam and HYDROS systems, primarily for benign prostatic hyperplasia (BPH) treatment. Stryker ranks third with its Mako system, which is widely used in orthopedics for

knee and hip arthroplasty. In the Surgical Navigation Market, Medtronic holds the leading position, followed by Brainlab and Stryker. Surgical navigation systems are widely used in neurosurgery, orthopedic procedures, and ENT (Ear, Nose, and Throat) surgeries to enhance precision and outcomes. These systems utilize advanced imaging and tracking technologies to assist surgeons in real-time, reducing errors and improving surgical efficiency [4].

The field of robotic-assisted spine surgery has evolved significantly over the past years. Companies are competing to advance precision, safety, and efficiency in spinal procedures. Among the leading solutions in the market are ExcelsiusGPS (Globus Medical), ROSA Spine (Zimmer Biomet Robotics), Cirq (BrainLab), and Mazor X (Medtronic). These systems offer advanced navigation and robotic assistance, enabling minimally invasive techniques [5]. However, it is important to note that these systems provide guidance; they do not drill holes or insert screws. The surgeon performs these tasks using specialized tools, relying on the trajectory indicated by the robotic arm's end effector.

Optical navigation forms the foundation of most modern robotic spine systems. These systems utilize infrared cameras to track reflective markers placed on the patient and surgical instruments, creating real-time spatial mapping of the surgical field. One example of a robotic spine system is the ExcelsiusGPS. The approach employs a dynamic reference base (DRB) attached to the patient's posterior superior iliac spine, serving as the primary spatial reference point. An additional surveillance marker detects unintended movement. The optical tracking system monitors the DRB and robotic arm's position. Such design allows greater adaptability to patient position changes during surgery. The surgical tools, equipped with reflective markers (frames), are guided through the robotic arm's end-effector following pre-planned trajectories. These marker frames enable real-time tracking of tool movements.

However, successful optical tracking depends critically on maintaining clear sightlines between cameras and reference markers throughout the procedure [5].

The Mazor X represents a combination of two approaches. The system combines optical tracking with mechanical stability. The robotic system is mounted to the table and physically connects to the patient via a pin placed in the posterior superior iliac spine (PSIS) or through a spinous process reference clamp. This mechanical linkage provides stability by creating a direct connection between the robotic arm and the patient's anatomy. The system uses a camera ("Mazor eye") for optical registration along with fluoroscopic imaging to create a 3D surgical plan. Similar to the ExcelsiusGPS system, the Mazor X guides surgical tools through its end effector along pre-planned trajectories. The Mazor X combines optical tracking and mechanical stability to overcome the limitations of purely optical systems, especially in cases where line-of-sight is compromised. However, once the system is mounted, it cannot maintain stability if the patient's position changes significantly during surgery [5].

Another approach in robotic assisted surgery includes augmented and virtual reality systems or machine vision technology; however, machine vision is limited to open surgery procedures. To confirm the placement of the screw fluoroscopy or CT scan is usually performed at the end of the surgery [6] [7].

Ultrasound navigation has also been explored as an alternative for navigation in MIS, providing real-time imaging without radiation exposure. The system combines a robotic platform with ultrasound imaging and drilling capabilities for pedicle screw placement. A linear probe is used for visualization, while the robotic system—equipped with force/torque sensors and custom-designed probe holders—enables precise control and positioning during

the procedure. Experimental studies have shown promising results. Integration of two systems gives the potential to improve the safety of patients and clinical results [8].

Moreover, there has been research on automated polyaxial screw placement using a robot. This system can perform autonomously and with high accuracy. The system was tested based on the internal system of a robot; no external navigation was used, which might lead to error due to the movements of a patient in real surgical conditions [9].

Magnetic navigation systems represent a transformative approach in minimally invasive medicine, with their ability to control medical devices through biological tissues without radiation exposure or line-of-sight constraints. A good example is the capsule endoscopy tracking system, where Hall Effect Sensor (HES) arrays are arranged in a 5x5 matrix [10].

Another example is the electromagnetic navigation system Navion, which precisely controls magnetic materials and devices for minimally invasive procedures. By generating controlled magnetic fields, Navion can steer magnetic catheters, microrobots, and particle swarms inside the body, enabling targeted drug delivery, neurovascular interventions, and endovascular treatments. This technology enhances precision and safety, allowing doctors to navigate narrow blood vessels, delicate brain structures, and other hard-to-reach areas [11].

Commercially available electromagnetic tracking systems like the NDI Aurora provide real-time tracking of microsensors embedded in medical instruments such as catheters, endoscopes, and needles. Operating without requiring line-of-sight, it enables precise tracking through anatomical structures. The system integrates with image-guided surgery platforms, allowing medical professionals to visualize instrument positions during minimally invasive procedures, making it widely used in interventional procedures, biopsy guidance, and surgical navigation [12].

This project hypothesizes that accurate localization of the drilling angle and pedicle screw placement in minimally invasive spine surgery can be achieved **without relying on optical tracking** or long-distance traveled by **combining Ultra-Wideband (UWB) technology with magnetic navigation**. UWB ensures reliable spatial tracking over a broader area, while magnetic navigation provides high-precision guidance in close proximity. This hybrid approach enhances the accuracy and efficiency of robotic-assisted pedicle screw placement, potentially reducing complications and improving clinical outcomes.

The proposed hybrid system is designed to guide robots through mini-invasive surgery of the thoracolumbar spine while using robots for drilling and placing pedicle screws. Figure 1 illustrates the navigation concept[1], presenting the integration of UWB and magnetic sensing.

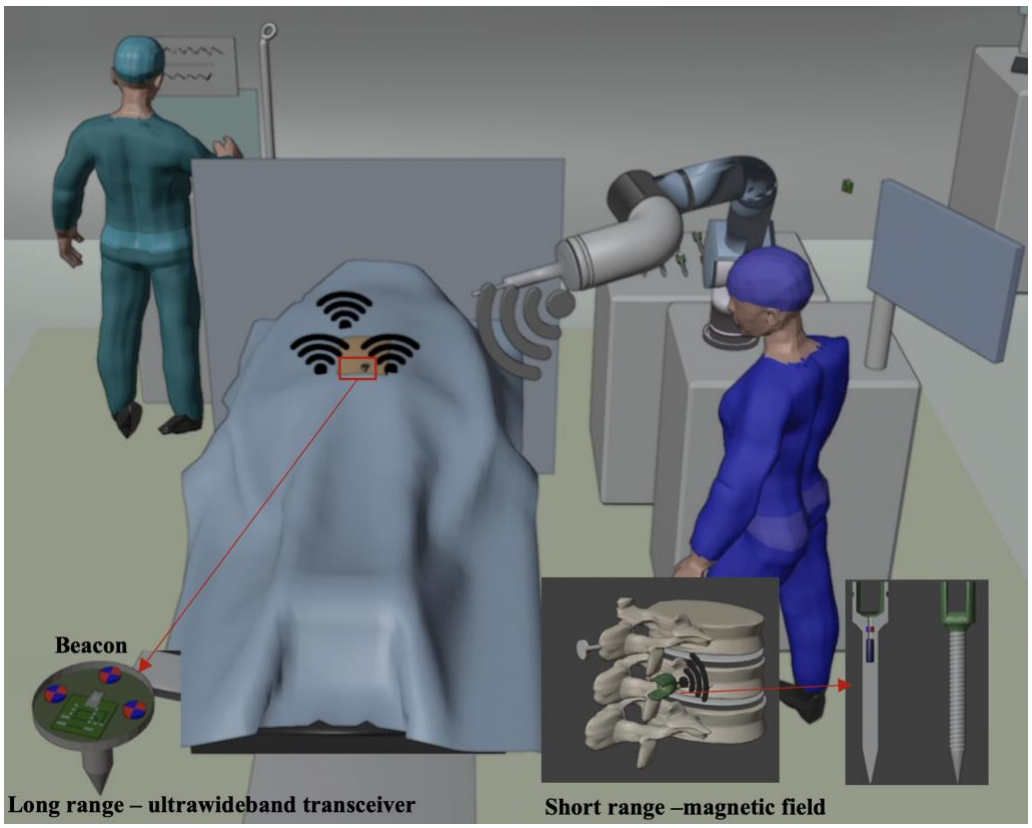

Figure 1. Hybrid navigation concept

[1] *Hybrid Navigation*, YouTube [https://youtu.be/rm-NIdTIgLs]

Figure 2 shows a conceptual diagram illustrating the placement of the three beacons on a patient, the robotic arm equipped with both UWB tag and magnetic sensors, and the range of motion of the robotic arm around the screw. This figure presents the core principles of the navigation system, showing the integration of UWB and magnetic sensing technologies for accurate robotic guidance.

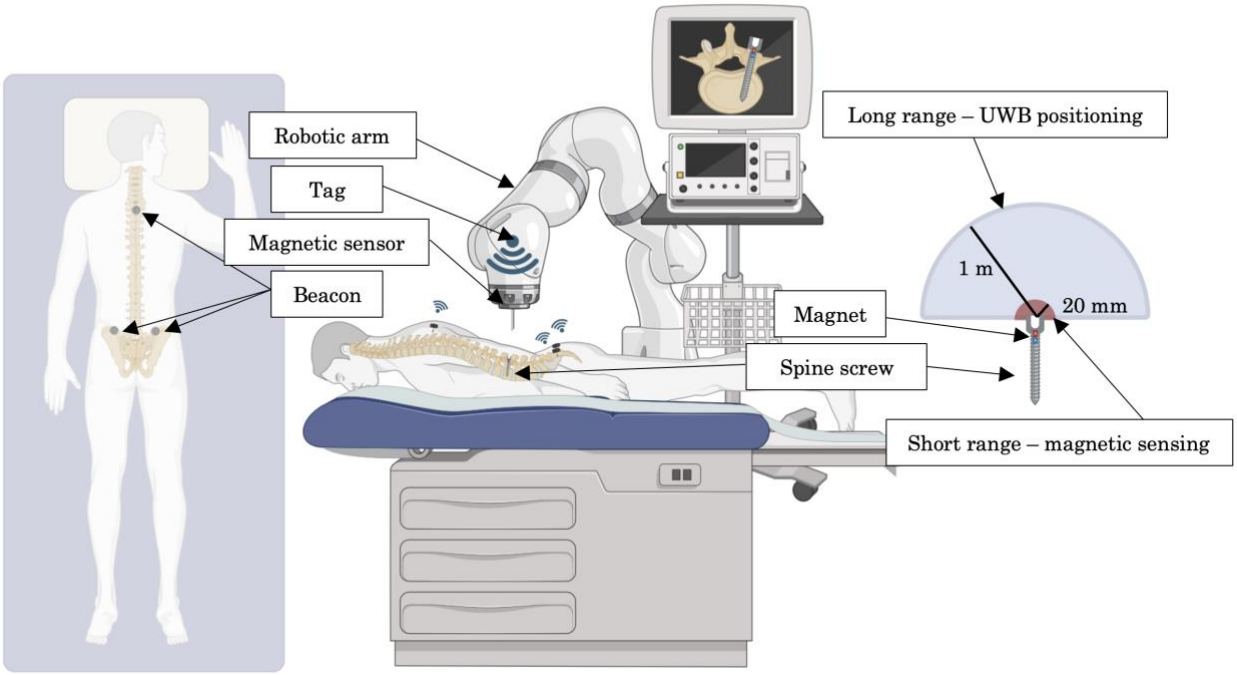

Figure 2. Conceptual diagram of the surgical setup and elements of the system

While four removable beacons would be required for complete 3D positioning, this proof-of-concept implementation uses three beacons in a triangular configuration on a patient's spine/iliac to validate the fundamental principles of the UWB navigation system in 2D. Beacon includes an ultrawideband transceiver functioning as an anchor. According to the concept, each of the beacons would be equipped with three permanent magnets working as magnetic markers and reference points for the magnetic sensing system. This work simplified the setup to three beacons, allowing to verify the core functionality of UWB positioning before expanding to full 3D capabilities and magnetic sensing integration.

The navigation module, consisting of a magnetometer and ultra-wideband transceiver (tag), is attached to the robotic arm. The tag enables the determination of the location of the robotic arm according to the spine of the patient in a longer distance range, using trilateration of UWB modules based on the time of flight (ToF) method.

This project comprises screw equipped with permanent magnets integrated into the body of a screw, allowing to detect the location of the screw in relation to a spine of a patient, including angulation. In the concept, the screw visualization is performed in 3D software, depending on the input parameters of the screw, such as diameter and length established by a surgeon. The advantage of this system over existing navigation solutions in robotic applications is its ability to control screw positions using magnetometer readings, which are not affected by line-of-sight issues. Unlike optical navigation systems, which can be disrupted by obstacles, this system ensures reliable tracking in such conditions. Additionally, the system does not require fluoroscopy images while performing surgery and leverages the complementary strengths of UWB and magnetic sensing to overcome line-of-sight limitations, reduce radiation exposure, and provide high-precision navigation in dynamic surgical environments.

Beacons at this point are designed to be removable devices. Research according to implantable devices, which could be implemented in the future, should be done. While reviewing implant communication technologies in the wireless body area network (WBAN), various technologies are considered, including antenna-based RF, inductively coupled data transfer, body channel communications, molecular communications, optical communications, and ultrasonic communications. Each of these methods presents unique advantages and limitations in terms of range, frequency, and standardization, as outlined in Table 1. Evaluating these technologies will help determine their feasibility for future implantable

beacon systems, ensuring reliable communication while minimizing power consumption and biocompatibility concerns.

Technology	Method of propagation	Range	Frequency	Standard
Antenna based RF	Radio wave propagation	2 m	401 - 406 MHz, 2.36-2.4 GHz	MedRadio / MICS
Inductively coupled data transfer	Magnetic field (Mutual Inductance)	a few cm (<4 cm)	1,2,5,10,24,49 MHz	none
IBC - body channel communications	Electric field	body confined (<10 cm for implants)	Galvanic < 10 MHz, Capacitive 21 MHz	IEEE Std. 802.15.6
Molecular Communications	Action potential, Axon propagation, ionic diffusion through junction gap, Hormone diffusion through blood	nm -µm	(0,3 kHz)	none
Optical Communications	Infrared propagation	mm (mostly subcutaneous <4 mm)	700 nm - 1 mm (300 GHz - 430 THz)	none
Ultrasonic Communications	Ultrasonic propagation	Several centimeters (≈10 cm)	1-3 MHz	none

Table 1. Implant communication technologies [13]

Ultra-wideband (UWB) technology offers a promising solution for indoor localization because of its high wave directivity and high-frequency operation, which minimize multipath effects. In line-of-sight (LOS) conditions, UWB systems can achieve good positioning accuracy using time-of-flight measurements between anchors and tags. The effectiveness of UWB localization depends significantly on anchor placement. UWB systems with four anchors can achieve 3D positioning accuracy within centimeters.

Indoor positioning and navigation technologies have advanced significantly, offering diverse solutions for precise location tracking in enclosed spaces. Figure 3 presents a detailed comparison of five key positioning technologies: Ultra-Wideband (Qorvo UWB), Bluetooth, WiFi, RFID, and GPS, evaluated across ten critical performance metrics.

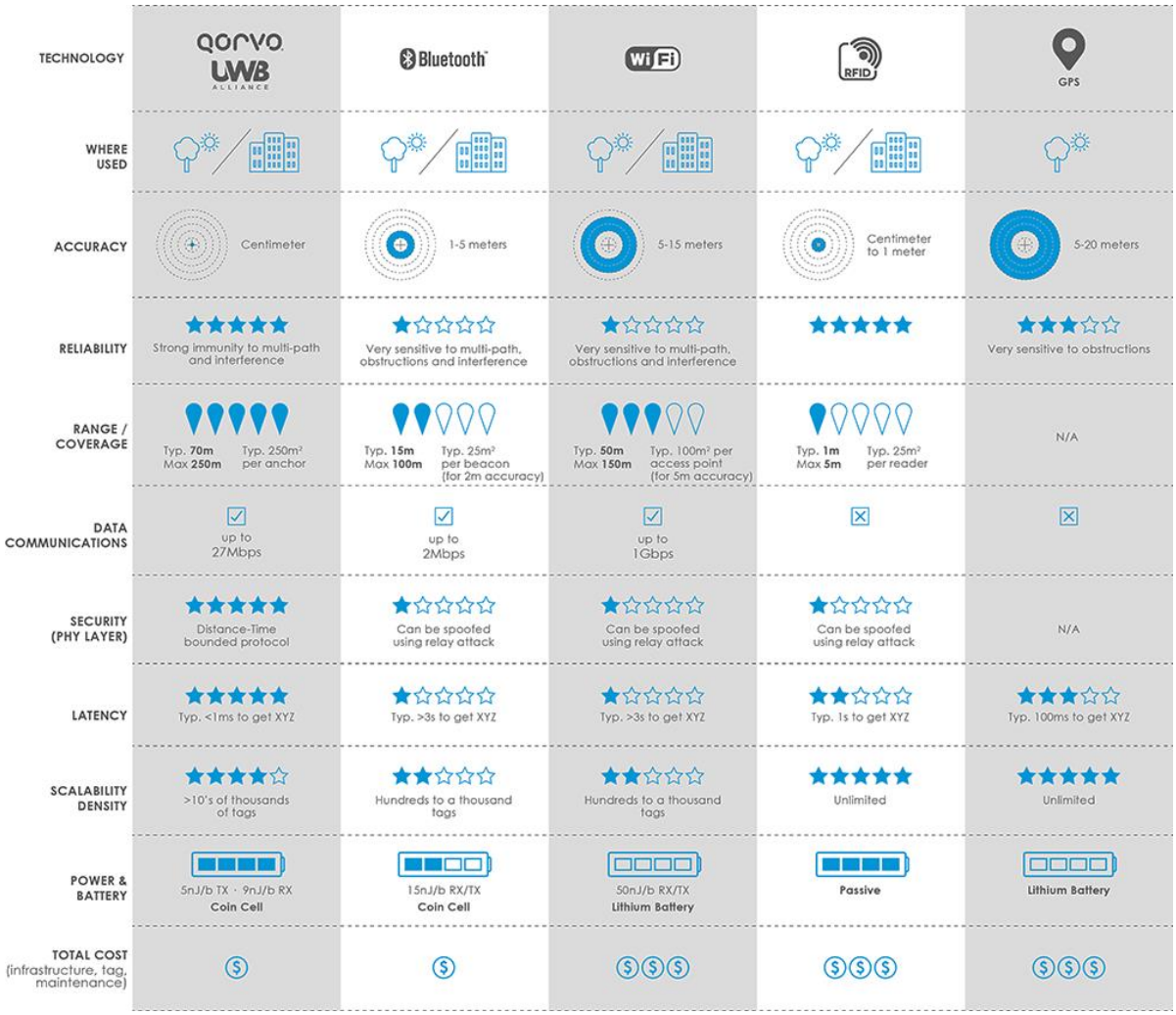

Figure 3. Positioning technologies – comparison [14]

The comparison highlights the advantages of UWB for indoor applications. In terms of precision and adaptability, UWB achieves centimeter-level accuracy, outperforming Bluetooth's 1-3 meter range, WiFi's 3-15 meter range, and other technologies that vary in accuracy based on environmental conditions. UWB functions effectively in both indoor and outdoor environments while demonstrating superior resistance to multipath interference and obstacles.

While both magnetic navigation and UWB technology offer advantages, they have limitations when used alone. Magnetic navigation provides high precision in close proximity

but is limited to short-range operation. UWB technology, although capable of operating at much longer ranges, provides centimeter-level accuracy which may not be sufficient for precise surgical navigation. Combining these approaches could overcome the limitations of both navigation systems and individual technologies, leveraging magnetic sensing for high-precision close-range guidance while using UWB for broader spatial tracking. Moreover, with the proper software, a fully automated system could be used for telemedicine applications under circumstances when expertise from another surgeon is required.

This system lays the groundwork for advancements in surgical robotics and telemedicine, enabling remote assistance, reducing surgical time, and expanding access to minimally invasive procedures in resource-limited settings. The proposed solution combines UWB and magnetic navigation on a larger scale, but further work is needed to optimize its size, range, and precision before it can be applied in clinical settings.

The project aims to design a system with UWB navigation maximum root mean square error (RMSE) of 5 cm and magnetic navigation to measure the angle of the magnet (θ) with a mean absolute error (MAE) below 5° and a distance mean absolute error of 1 μm.

2. Materials and methods

2.1. Ultra-wideband (UWB) positioning system

The system is designed as a 2D UWB navigation, simplifying its full 3D potential to serve as a proof of concept. Although full 3D navigation is the ultimate goal, the 2D approach used in this phase allows for effective validation of important concepts, like combining magnetic and UWB navigation for accurate positioning. The implementation assumes line-of-sight conditions and does not include Fresnel zone considerations.

2.1.1. Hardware

The hardware setup consists of 2 ESP32 and 2 ESP32 Pico D4 microcontrollers integrated with Qorvo DW1000 transceivers for long-range communication. Each module can function as both a tag and an anchor. These chips are cost-effective and energy-efficient, supporting six channels ranging from 3.5 to 6.5 GHz, with data transfer rates of up to 6.8 Mbps. In this implementation, Channel 5 (6.5 GHz) was used with a data rate of 110 kbps. Transceivers have embedded antennas (module DWM1000/BU01) and communicate with the host processor through the SPI interface. According to the manufacturer, the precision of measurements can reach up to 0.1 meters. This ultrawideband chip is compliant with IEEE 802.15.4-2011 standards (IEEE Standard for Local and Metropolitan Area Networks, Part 15.4: Low-Rate Wireless Personal Area Networks (LR-WPANs)). The wireless communication standard defines the physical (PHY) and medium access control (MAC) layers for low-power, low-data-rate wireless networks [15].

Communication between the tag and anchor utilizes the simple Single-Sided Two-Way Ranging (TWR) method to calculate the Time of Flight (ToF). The ToF is the duration

required for the signal to travel between the initiator and the responder. The initiator transmits a signal to the responder, which, upon reception, sends a response back to the initiator [16]. The scheme of ranging is presented in Figure 4. The orientation between DW1000 modules affects ranging accuracy.

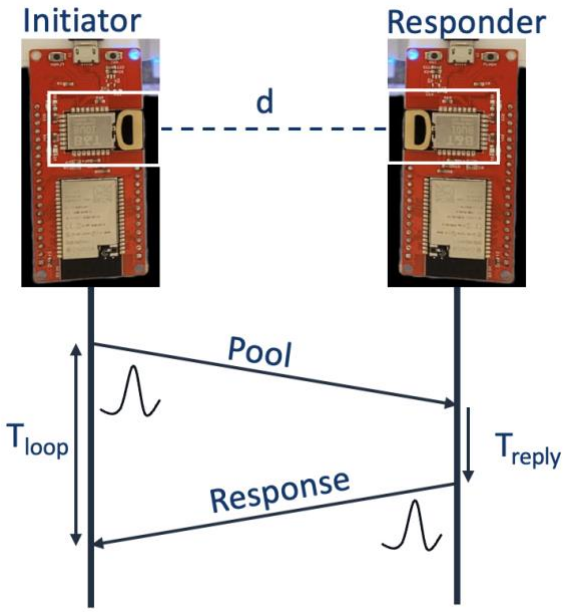

Figure 4. Schematic of Two-Way Ranging, ESP32 with DW1000 transceivers

The distance between antennas is calculated using Time of Flight (ToF), derived from round-trip measurements (1), and then multiplied by the speed of light (2). This method provides more accurate results than one-way ranging as it eliminates the need for precise time synchronization between devices.

$$ToF = \frac{T_{loop} - T_{reply}}{2} \quad (1)$$

$$d = ToF * c \quad (2)$$

The direction of the DW1000 antenna can influence signal strength and reliability. Proper antenna positioning is essential to ensure accurate ranging.

2.1.2. Trilateration

In this project, three anchors and one tag are employed. The positions of the anchors are predetermined, while the position of the tag (x, y) is calculated using the trilateration method. Unlike triangulation, which determines position based on measured angles, trilateration relies on the distances between the tag and the anchors. Triangulation relies on angle measurements, typically using directional antennas or angle-of-arrival (AoA) sensors to measure the angles between the target and reference points. Triangulation and trilateration are two essentially different methods for determining a position [17].

Trilateration is a technique used to determine an unknown position through measurements of the distance to three known points (tag–anchor). Circles are drawn around them in the known positions with the same radius as the measured distance. For each measurement, the unknown position is somewhere along the circumference of the circle. As it is valid for each circle, the position of a tag can be determined as the point where the circles intersect [18]. The schematic of the trilateration is presented in Figure 5. If the circles do not intersect at one point due to measurement errors, then the unknown position may be assumed to be where the circles overlap.

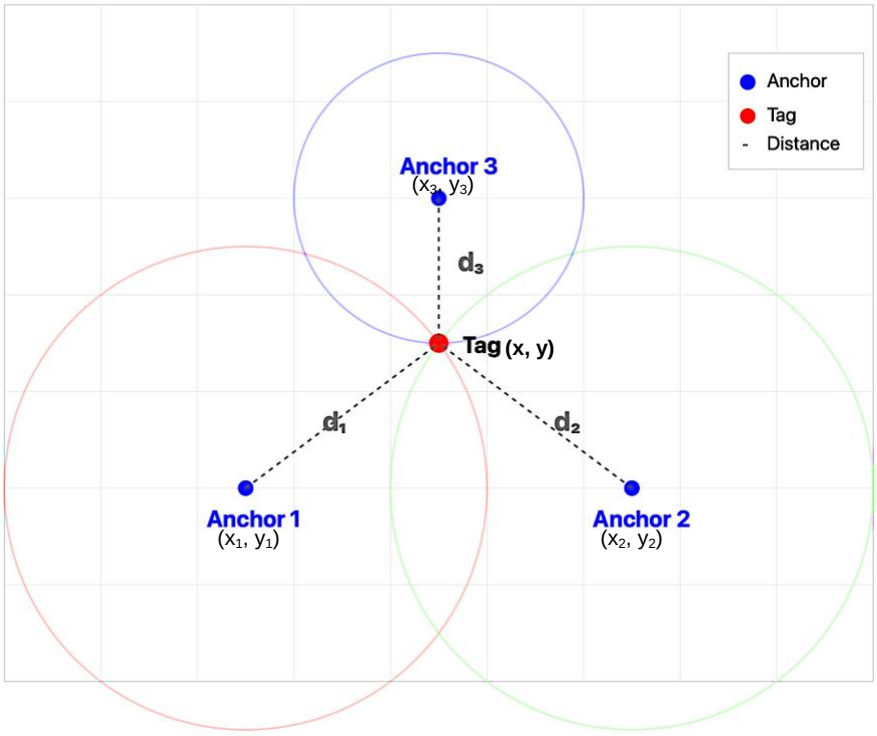

Figure 5. Trilateration method - graphical representation

The analytical solution is based on the solving equations of the three circles and the intersections between them (3) [18].

$$\begin{bmatrix} (x-x_1)^2+(y-y_1)^2 \\ (x-x_2)^2+(y-y_2)^2 \\ (x-x_3)^2+(y-y_3)^2 \end{bmatrix} = \begin{bmatrix} d_1^2 \\ d_2^2 \\ d_3^2 \end{bmatrix} \quad (3)$$

2.1.3. Testing setup

The testing setup of 2D UWB positioning is presented in Figure 6a, for longer distance ranging. The grid 2 x 2 [m] was prepared with increments of 0.5 m. 3 anchors placed in positions: Anchor 1 (0.0, 0.0), Anchor 2 (2.0, 0.0), Anchor 3 (1.0, 2.0). For measurements, 9 different points were considered: (0.5, 0.5), (0.5, 1.0), (0.5, 1.5), (1.0, 0.5), (1.0, 1.0), (1.0, 1.5), (1.5, 0.5), (1.5, 1.0), (1.5, 1.5). The transceivers DW1000 were placed 10 cm above the ground.

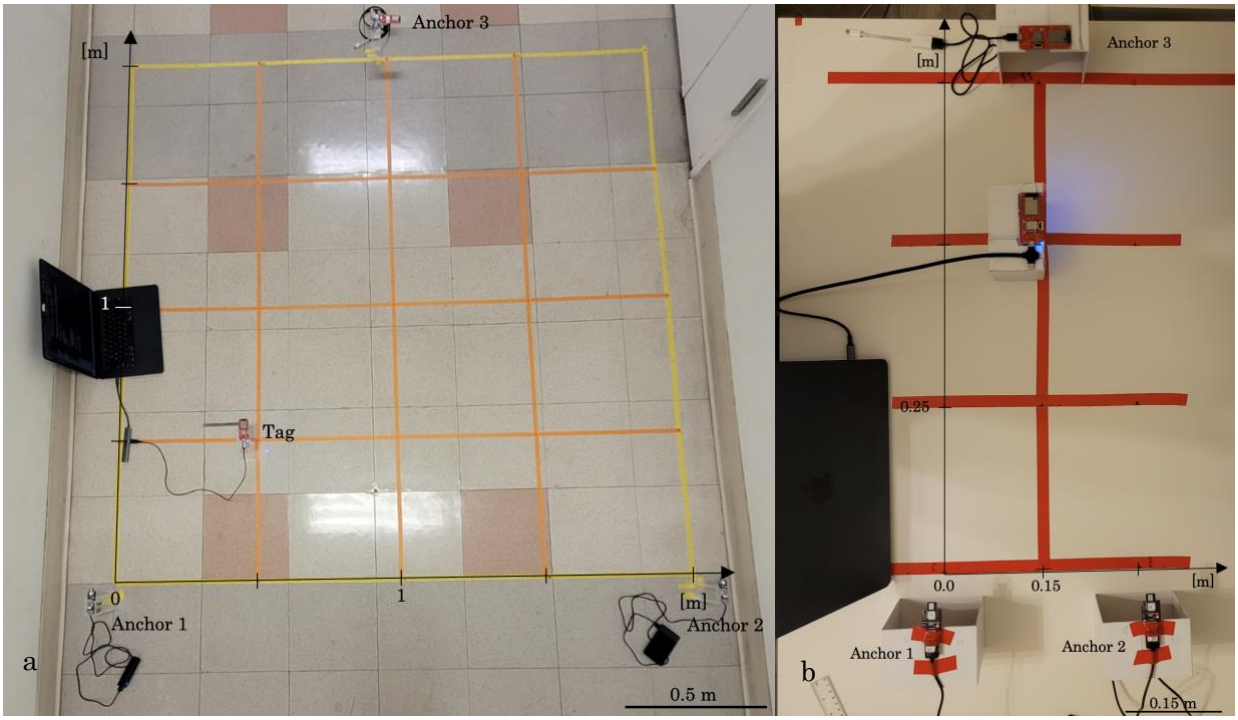

Figure 6. Testing setup for 2D UWB positioning system a) long range, b) medium range

For longer range testing, the GUI (Graphical User Interface) was created, based on Python code, to display the real-time location of the tag. The GUI was designed to enable setting the target position and desired distance around the specified point.

After performing the long-range tests, a second set of measurements was conducted at medium distances relevant to surgical applications. Anchor 1 was placed at 0,0, Anchor 2 at 0.30, 0 and Anchor 3 at 0.15, 0.75 [m]. 6 different points were tested: (0.0, 0.25), (0.0, 0.50), (0.15, 0.25), (0.15, 0.50), (0.30, 0.25), (0.30, 0.50) [m]. The setup is presented in Figure 6b.

2.1.4. Errors and data filtering

The distances measured by the ESP32/ESP32 Pico D4 DW1000 chip were not accurate at first. To improve measurements, 500 distance measurements were collected three times between each anchor and tag at each point (nine points for the longer range, six points for

the medium range). Excel was used to approximate a correction polynomial for each anchor. The correction polynomial is a function that gives the corrected value as a result of inputting the measured value. Additionally, data out of range of the device were filtered out and a moving average filter was used to smooth the receiving data and reduce noise with a window size of 8. Data were processed by using Python code. After applying a filter, a set of three of 100 data points was collected from each measurement point.

The error of the positioning system was determined by root mean square error (RMSE) (4). This was performed for static measurements.

$$\mathrm{RMSE} = \sqrt{\sum_{i=1}^{n} \frac{(\hat{y}_i - y_i)^2}{n}} \tag{4}$$

Where:

$\hat{y}_1, \hat{y}_2 \ldots \hat{y}_n$ predicted values

$y_1, y_2 \ldots y_n$ observed values

n number of observations

2.2. Magnetic sensing system

Magnetic navigation is designed to detect the theta angle of the magnetic field vector, indicating the angular position of a magnet embedded in surgical screws. While UWB provides broader positioning capabilities, magnetic navigation offers high-precision detection at close range. The current approach to magnetic field detection involves generating synthetic data of the magnetic field around the magnet and creating a 3D database with vector field components. This method relies on measuring the magnetic field vector components in three-dimensional space, which change as the position of the magnet changes. The system uses

spherical coordinates to describe the magnet's position relative to the sensor, with the angular measurement (θ) being critical in determining the magnet's orientation. Through careful calibration and comparison with known reference points, the system can determine the orientation of the magnet relative to the sensor. Magpylib was selected as the primary simulation tool due to its computational efficiency and ease of implementation.

A 3D map of the magnetic field was generated by Magpylib[2] – an open source Python package for calculating static magnetic fields of magnets. The process involves mapping the magnetic field around a cylindrical permanent magnet over the grid, representing the magnetic field around the magnet embedded in the spine screw.

The cylindrical magnet was simulated to be magnetized to 1 144 324 A/m along its z-axis and has dimensions of 1.59 mm in diameter and 6.37 mm in height. By rotating the magnet in 1° increments from 0° to 46° θ, the simulation creates an extensive dataset of magnetic field properties. The limitation of the theta angle is due to the limitations of the computer memory to process a big set of data.

The intensity of the magnetic field decreases rapidly with increasing radial distance from the magnet. The magnetic field is more complex, close to the magnet, and with distance, follows the inverse cubic relationship. Therefore, three different grids were used: close to the magnet (z up to 5 mm) - dense grid with a resolution of 0.25 mm, further apart (z up to 10 mm) moderate grid with a resolution of 0.5 mm, and a coarse grid (z up to 20 mm) with a resolution of 1 mm. A side view of the generated grid is presented in Figure 7. Each point of the grid has three magnetic field components - B_x, B_y, and B_z corresponding to values on the x, y, and z-axis. To ensure the simulation accurately represents real-world conditions, noise

[2] https://magpylib.readthedocs.io

generation was added based on the datasheet specifications of the gaussmeter available in the lab - Lake Shore F71. Gaussian random distributions were used to simulate data reading noise (0.3% of the measured value) and system noise (0.16 μT), creating a realistic representation of sensor measurement errors.

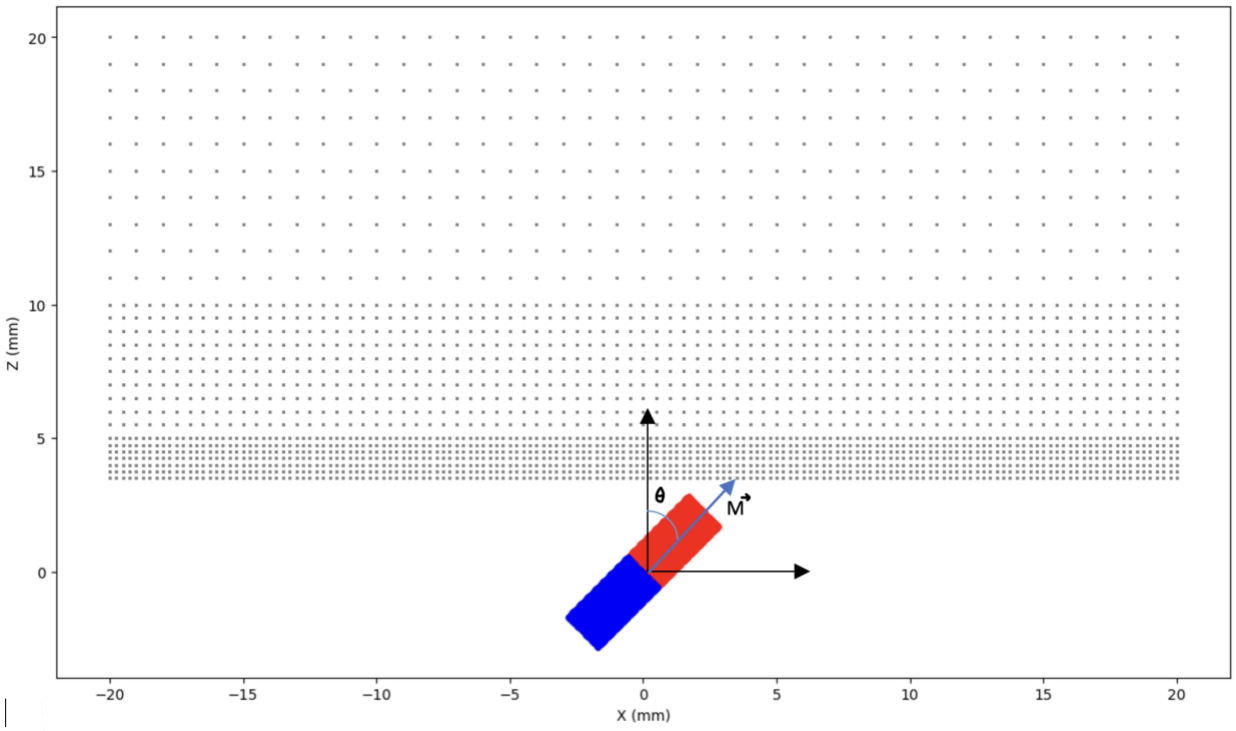

Figure 7. Side view of the generated grid and magnet representation for theta=45°

For validation purposes, a parallel simulation using COMSOL 6.2 was performed to verify the accuracy of the generated data.

2.2.1. Hardware

To compare synthetic data with the real model, the measurements along the z-axis were performed by using the gaussmeter Lake Shore F71 with a Hall probe to sense the magnetic field. The setup of the measurements is presented in Figure 8. A stand with a magnet was placed in a holder to ensure the correct position. The gaussmeter probe was attached to the

gantry of the CNC machine NOMAD 3, by a 3D printed handle. By use of the CNC software, precise movement (along the z-axis) of the gaussmeter probe was possible.

The gaussmeter provides three-dimensional sensing with direct measurements of the x, y, and z components of the magnetic field. The magnet used in this experiment is a neodymium cylinder magnet (grade N52) with a 1.59 mm diameter and 6.37 mm thickness. According to the manufacturer, the sensitive area of the probe of the gaussmeter for the B_z is 0.35±0.3 mm. The value 0.35 mm was assumed to be the correct value.

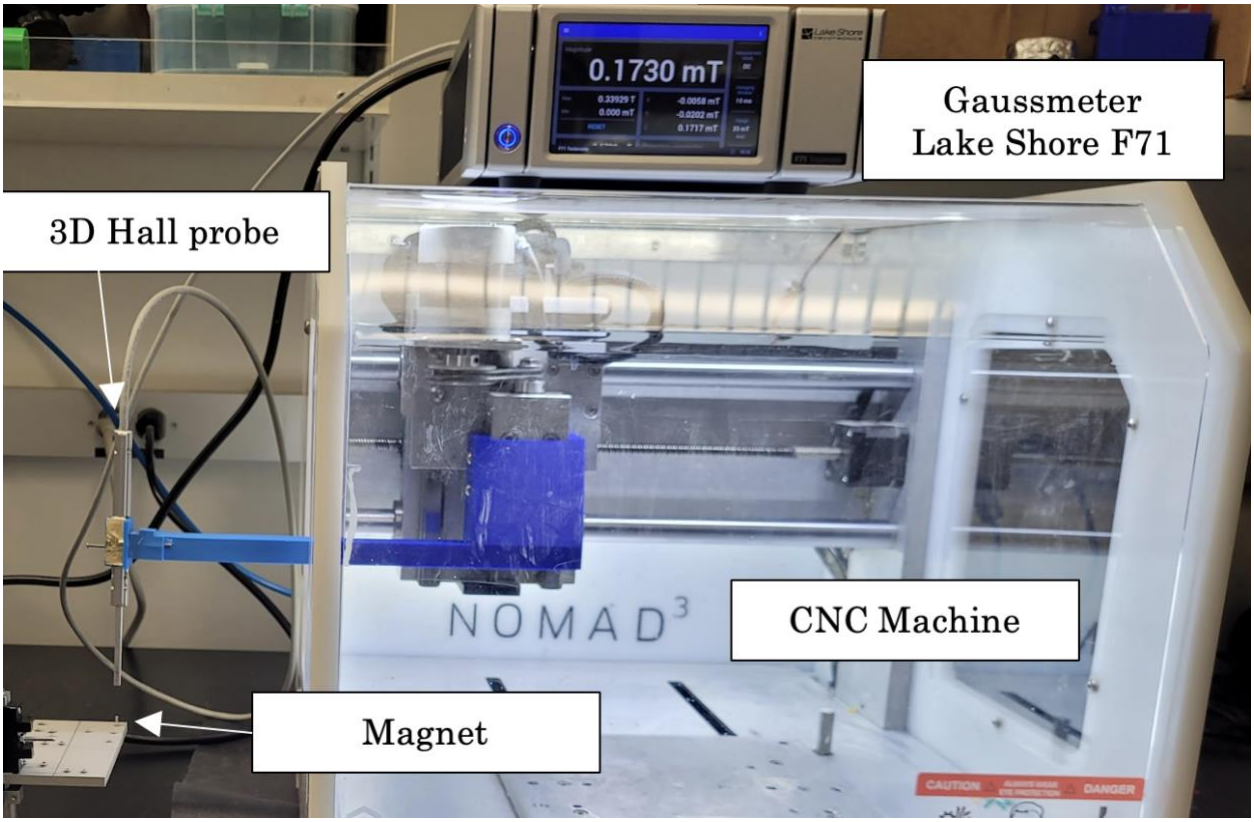

Figure 8. Magnetic field measurement setup

2.2.2. Machine learning

The data generated by Magpylib were used to train a model to detect the angle of the magnetic field and the distance from the sensor to the center of the magnet, based on B_x, B_y, and B_z values. The single-sensor approach was initially used.

The neural network[3] was designed to process magnetic field measurements, taking three components (B_x, B_y, and B_z) in Tesla (mT) as inputs, and predicting both the magnet's angle in degrees and its distance in millimeters. The machine learning workflow diagram is presented in Figure 9. The algorithm used for both angle and distance predictions was GradientBoostingRegressor. The algorithm builds a sequence of decision trees, where each new tree learns from and corrects the mistakes of previous trees, and the final prediction is a combination of all trees' predictions working together. The models use 100 trees, a learning rate of 0.1, and train on 80% of randomly selected data for each tree. 20% of the data are used for testing. The angle model uses slightly deeper trees (depth=8) than the distance model (depth=6), with both requiring at least 50 samples to split a node.

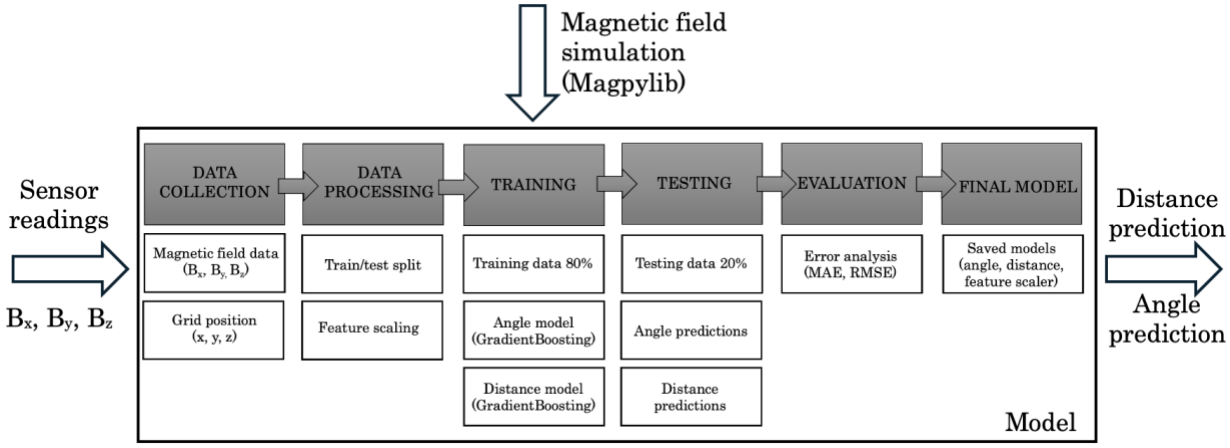

Figure 9. Machine Learning workflow diagram

[3] https://github.com/galkasylvia/Hybrid-Navigation

The model was trained on a comprehensive dataset consisting of 12 401 749 total points, which was split into a training set of 80% points and a test set of 20% points, ensuring robust validation of the model's performance. Each data point includes magnetic field components (Bx, By, Bz) and the corresponding position coordinates (x, y, z) and angle (theta)

The raw magnetic field data (B_x, B_y, B_z) was transformed to include total magnitude, field angles (θ_B, φ_B), and normalized components of the magnetic field. Data was processed in chunks of 100,000 samples and standardized using StandardScaler.

To verify the trained models, additional testing was performed with 10^6 random points within trained ranges for different angles of the magnet. To get examples of predictions, the data of the magnetic field was generated at random distances from the magnet and selected angles (0°, 30°, 45°) of the magnet. After simulating new points in space, the model was loaded, and predictions were obtained based on magnetic field data (B_x, B_y, B_z).

Once the single-sensor approach was analyzed, there was a need to improve output, and a second reading was added to simulate the second sensor. The second sensor was designed to be 8 mm apart from the first sensor, the data for machine learning code for x values were filtered to be from -20 to 12 mm to cover generated data. The same parameters of machine learning were used as in the single-sensor code. To test the model, the values of the first sensor were used as in the previous test, while values for the second sensor were generated by Magpylib for x+8, y, and z to compare results.

3. Results

3.1. Ultra-wideband (UWB) positioning system

Graphical representations of position measurements for different points for long range are presented in Figure 10. Each of the tag coordinates is represented by a different color. The average values of the positions are marked on the plot by the 'x' tag.

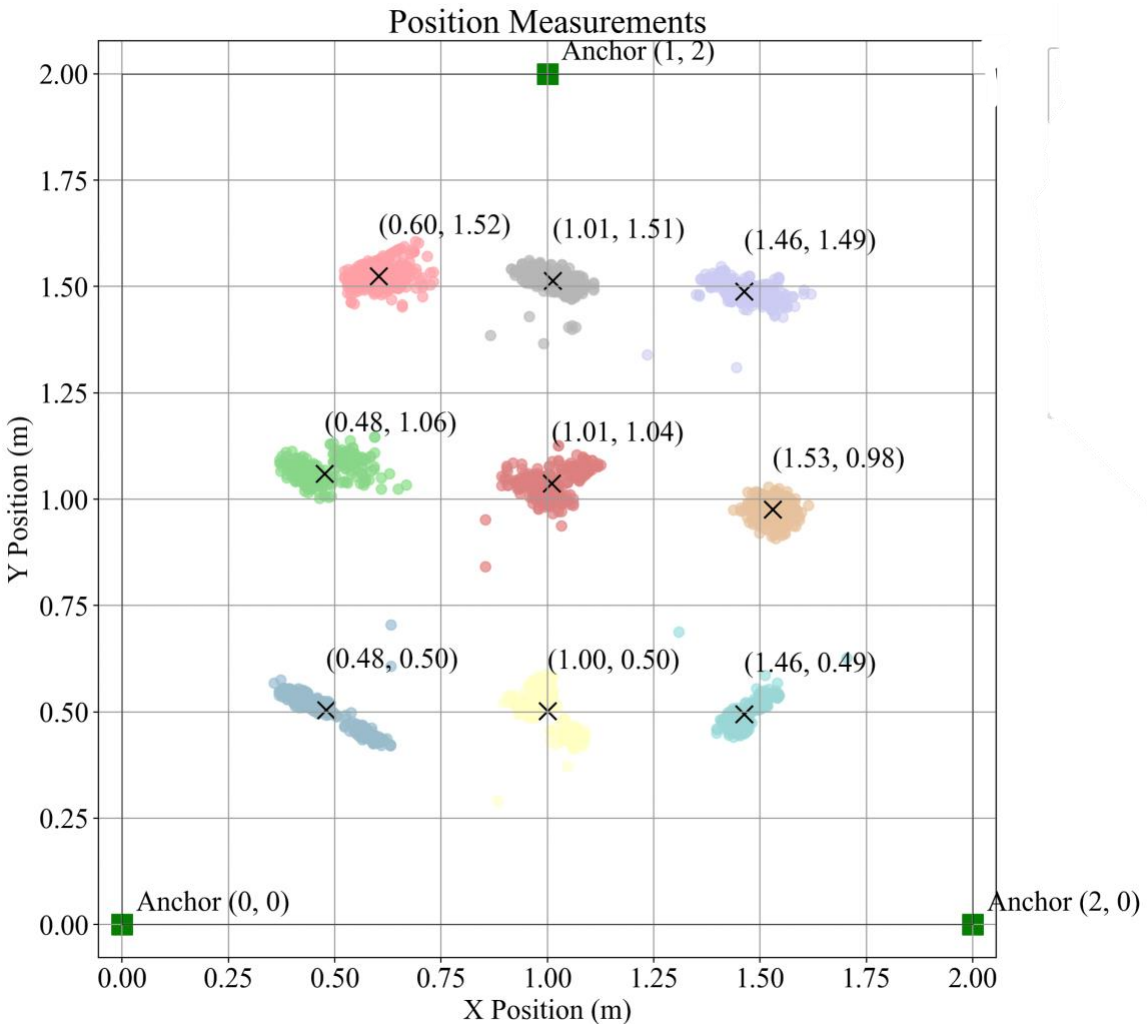

Figure 10. Position measurements for long range

Table 2 presents the average measured position for each actual position, along with the RMSE values for the x and y axes, over a long range. The average value of RMSE of all measurements (in both x and y-axis) is 5.3 cm (6.3 cm for the x-axis and 4.2 m for the y).

Actual position [m]		Average measured [m]		RMSE [m]	
x	y	x	y	x	y
0.50	0.50	0.48	0.50	0.08	0.04
0.50	1.00	0.48	1.06	0.07	0.07
0.50	1.50	0.60	1.52	0.11	0.04
1.00	0.50	1.00	0.50	0.05	0.05
1.00	1.00	1.01	1.04	0.05	0.05
1.00	1.50	1.01	1.51	0.04	0.03
1.50	0.50	1.46	0.49	0.05	0.03
1.50	1.00	1.53	0.98	0.04	0.03
1.50	1.50	1.46	1.49	0.08	0.04

Table 2. The average measured value of x and y positions and RMSE for a longer range

Data for a medium range is presented in Table 3. The average RMSE value of both axes in this range is 4.4 cm (7.0 cm for the x-axis and 1.8 cm for the y-axis).

Actual position [m]		Average measured [m]		RMSE [m]	
x	y	x	y	x	y
0.00	0.25	0.02	0.25	0.03	0.01
0.00	0.50	0.14	0.46	0.14	0.04
0.15	0.25	0.16	0.26	0.02	0.01
0.15	0.50	0.22	0.50	0.07	0.01
0.30	0.25	0.22	0.28	0.08	0.03
0.30	0.50	0.22	0.50	0.08	0.01

Table 3. The average measured value of x and y positions and RMSE for a medium range

For the navigation application, the GUI interface was designed to display the current position of the tag (red dot) – Figure 11. It is possible to set the target position coordinates as well as the radius of the target where the tag should be moved. While reaching the target position, the information is displayed on the screen.

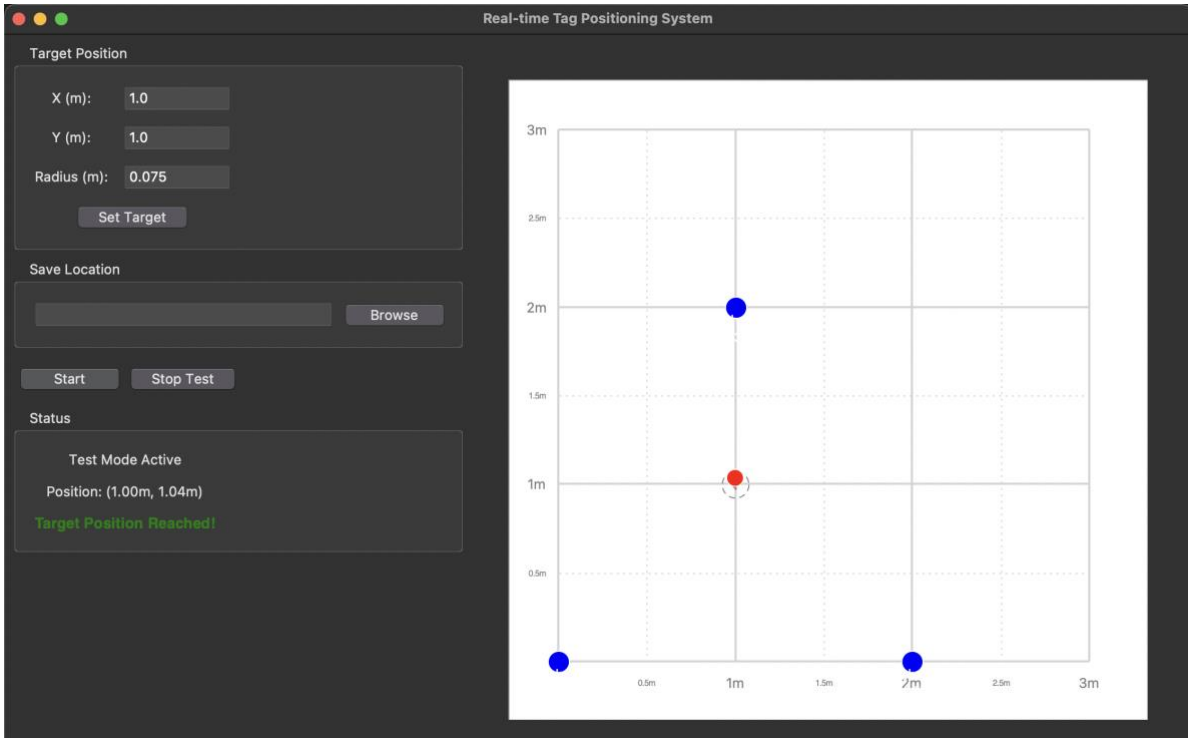

Figure 11. GUI for positioning system indicating reaching target position

3.2. Magnetic sensing system

An example of data generated by Magpylib, illustrating the representation of magnetic field lines along with a magnetic field map at a θ of 45°, is presented in Figure 12.

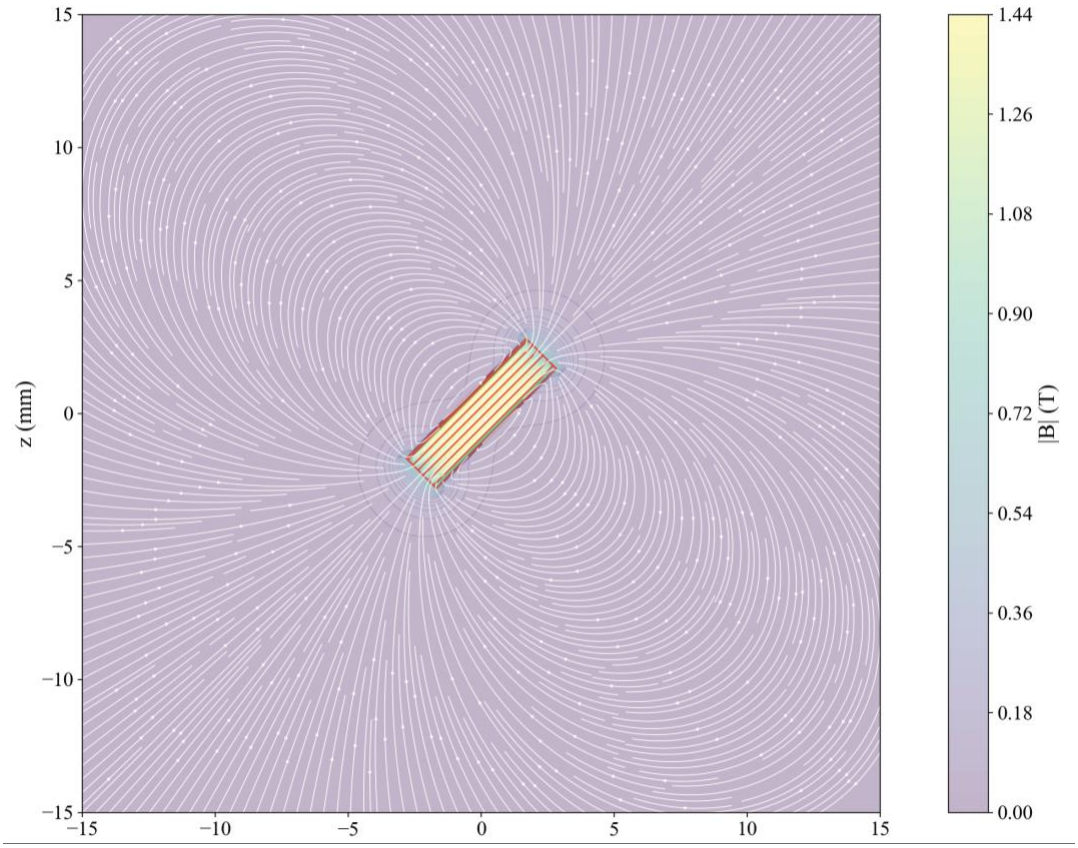

Figure 12. Magnetic field lines of a simulated magnet, theta 45°

Validation of the magnetic field model involved comparing theoretical predictions with experimental measurements. Figure 13 shows the comparison of B_z field values along the z-axis (x=0, y=0) between Magpylib simulation, COMSOL finite element analysis, and physical measurements using the Lake Shore F71 gaussmeter. The close agreement between these methods validates the accuracy of our magnetic field modeling approach.

Analyzing generated data by Magpylib, after analysis it was noticeable that the magnetic field for different angles might have the same values at different points in the space, thus causing ambiguity in the training process, leading to low performance in angles predictions.

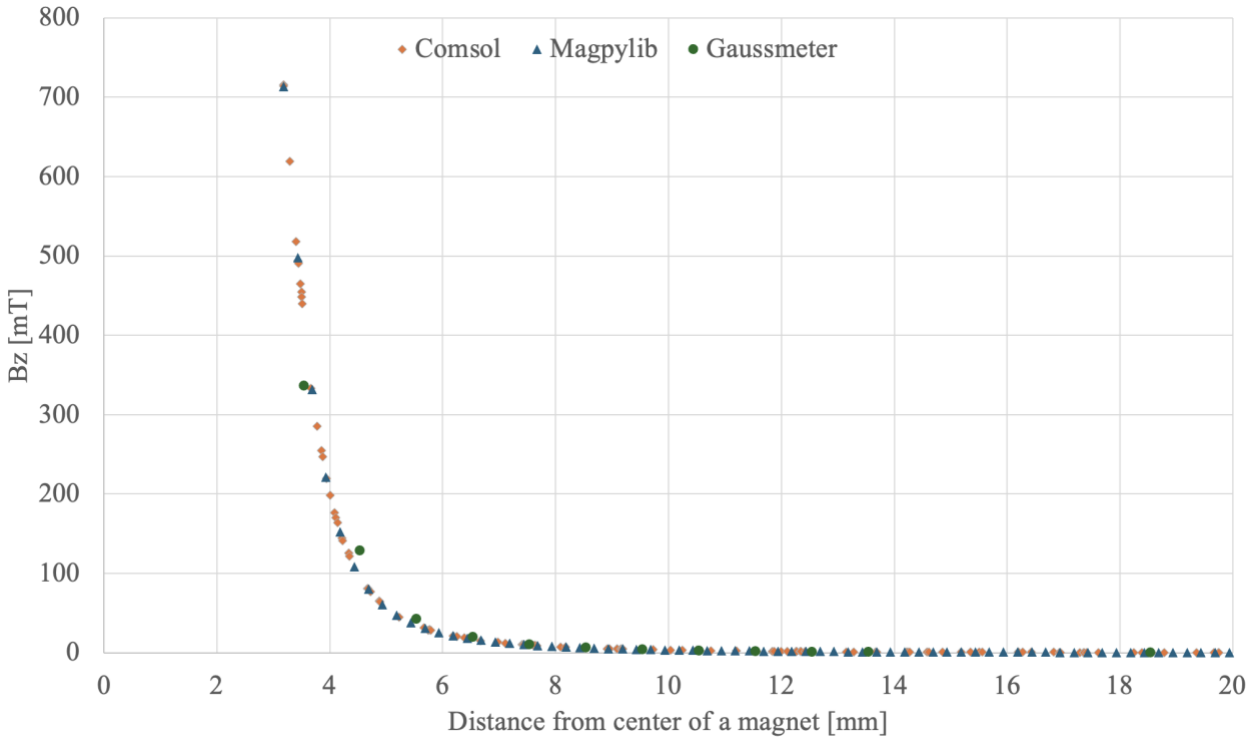

Figure 13. B_z value vs distance from the center of a magnet

For the single-sensor approach, the distance prediction achieved a mean absolute error of 150 µm, while the angle prediction exhibited less accuracy with a mean absolute error of 8.23°. However, after performing additional tests on the trained models, based on the 10^6 random points, the model's mean absolute error was 10.41° and distance error 240 µm, showing no consistency with the received analyses from the machine learning testing part. Examples of predictions based on the B_x, B_y, and B_z values for one sensor are presented in Table 4.

B_x [mT]	B_y [mT]	B_z [mT]	True angle [°]	Predicted angle [°]	Angle error [°]	True distance [mm]	Predicted distance [mm]	Distance error [mm]
-0.0494	-0.1186	-0.0115	0	16.69	16.69	24.84	24.42	0.42
0.5688	0.9787	1.0758	0	27.05	27.05	12.20	12.19	0.01

-0.6680	0.1218	-0.7867	30	25.42	4.58	10.76	10.78	0.02
-0.1487	-0.0061	0.0057	30	21.91	8.09	22.55	22.92	0.37
-0.0631	-0.0119	-0.0374	45	37.95	7.05	26.81	26.76	0.05
0.0716	-0.2149	0.0592	45	26.98	18.02	21.67	21.62	0.05

Table 4. Examples of predictions of angle and distance for one sensor

The MAE value for angle prediction after performing the machine learning test reached a value of 3.49° and 10 μm for distance predictions. For the independent test (based on 10^6 random points), the mean absolute error of angle prediction was 5.15° and 10 μm for a distance. Examples of predictions based on the B_x, B_y, and B_z values for two sensors are presented in Table 5. The reading from the first sensor is presented first, then the reading from the second sensor for the predictions.

B_x [mT]	B_y [mT]	B_z [mT]	True angle [°]	Predicted angle [°]	Angle error [°]	True distance [mm]	Predicted distance [mm]	Distance error [mm]
-0.0494	-0.1186	-0.0115	0	10.37	10.37	24.84	24.84	0.00
-0.0001	-0.1561	-0.0026						
0.5688	0.9787	1.0758	0	14.74	14.74	12.20	12.21	0.01
0.4708	0.2155	0.0948						
-0.6680	0.1218	-0.7867	30	25.11	4.89	10.76	10.76	0.00
-1.2731	3.7358	0.3637						
-0.1487	-0.0061	0.0057	30	24.46	5.54	22.55	22.55	0.00
-0.2443	-0.0222	0.2237						
-0.0631	-0.0119	-0.0374	45	36.27	8.73	26.81	26.81	0.00
-0.1052	-0.0684	0.0081						
0.0716	-0.2149	0.0592	45	28.57	16.43	21.67	21.66	0.01
0.0813	-0.0987	0.0210						

Table 5. Examples of predictions of angle and distance for two sensors

Based on the examples, although some of the presented cases showed a slight decrease in the performance of angle prediction, adding a second sensor's data for those cases might introduce unnecessary complexity or noise. The angle prediction error for the double-sensor approach decreased significantly for most of the cases. The performance of distance has improved as well.

4. Future work

The development of the hybrid navigation system for spine surgical robots has identified several areas for future research and development. The current work is a foundation for more advanced implementations.

The UWB navigation system requires expansion from its current 2D implementation to full 3D positioning capabilities. This involves adding a fourth beacon and developing more sophisticated algorithms for 3D tracking. Research is needed to optimize antenna placement and orientation, particularly to improve x-axis accuracy, which showed higher instability in current testing. Advanced filtering methods and deep learning algorithms should be investigated to reduce noise and account for interference typical in operating room environments. UWB should also be tested dynamically to assess its performance in real-world surgical conditions. The impact of the Fresnel zone on signal propagation when tags are placed on patients needs evaluation (between floor, patient, and antenna), as this could significantly affect system performance in clinical settings. The implementation of double-sided two-way ranging (DS-TWR) could provide improved accuracy by minimizing clock drift and delay errors.

The magnetic navigation system presents several opportunities for enhancement. Future work should extend the magnetic field modeling beyond the current 46° limitation to cover a full 360° rotation, providing comprehensive orientation detection. The sensor array configuration needs optimization through testing various arrangements of multiple sensors to improve angle prediction accuracy. More sophisticated machine learning algorithms should be developed to better handle the complex relationship between magnetic field

measurements and magnet orientation. The effects of environmental magnetic interference in surgical settings should be investigated to ensure reliable performance.

Hardware development represents an important component of future work, particularly focusing on three key elements: pedicle screws with embedded magnets, beacons, and an integrated robotic arm sensor module. The pedicle screw design should integrate permanent magnets while maintaining its structural integrity for spinal fixation. To improve readings, magnets could be arranged to create distinct magnetic field patterns that enable reliable position detection. The screw design should consider MRI safety implications.

The surgical beacon system needs refinement from its current prototype to a smaller version and, finally, clinical. This involves miniaturizing the UWB anchor modules and developing a sterile, disposable package that can be attached to the patient. The beacons should incorporate reference magnets for the magnetic navigation system, enabling integrated calibration of both positioning methods.

The robotic arm sensor module requires integration of both UWB and magnetic sensing capabilities in a compact package. This unified sensor system should combine multiple magnetic sensors with the UWB tag while maintaining high precision for both positioning systems. The module needs proper shielding from electromagnetic interference and should be housed in an enclosure suitable for surgical use.

5. Conclusions

We propose a combination of UWB (long range) and magnetic navigation (short range) system that offers the potential to enhance real-time mesoscale positioning for robotic arm, offering the precision and accuracy required in spine procedures. Accurate positioning is critical for patient safety and good clinical performance.

Testing of the UWB positioning system yields an average error of 4.9 ± 3.0 cm, RMSE (root mean square error) value combining long (2 m x 2 m grid) and medium (30 cm x 75 cm grid) range in both axes. We evidenced better accuracy along the y-axis than the x-axis with RMSE values of 3-7 cm for the y-axis versus 4-11 cm for the x-axis in the longer range, with this disparity increasing in medium-range tests (y-axis: 1-4 cm, x-axis: 2-14 cm). While most of the y-axis measurements met the self-target of 5 cm RMSE, the x-axis measurements showed higher irregularity and exceeded the goal in some cases, particularly at medium ranges. The differences between the results are possibly caused by the arrangement of UWB anchors or the orientation of antennas.

A single-sensor magnetic navigation system demonstrated a distance prediction error of 240 μm, while the angle prediction accuracy exhibited a mean absolute error of 10.41° (self-target requirement of 5°). This significant angular error indicates that a single-sensor approach is insufficient for precise orientation detection. This is primarily due to the inherent ambiguity in magnetic field measurements, where different positions and orientations can produce identical field component readings. To address this issue we simulate the process as having a second sensor shifted 8 mm in the x-axis, then the mean absolute error angle decreased to 5.15°. For distance prediction, the MAE (mean absolute error) reached the value of 10 μm.

We identify that optimizing machine learning algorithms or adding more sensors could improve angle prediction error even further. Multiple sensors would provide additional spatial information and field gradient measurements, potentially enabling the system to distinguish between ambiguous magnetic field configurations and improve the overall accuracy of orientation detection. As the work is limited to changes in the theta angle in a limited range, more data is necessary to confirm the received output.

References

[1] Y.-S. Lee, D.-C. Cho and K.-T. Kim, "Navigation-Guided/Robot-Assisted Spinal Surgery: A Review Article," *Neurospine,* vol. 21, no. 1, pp. 8-17, 2024.

[2] C. D. Vo, B. Jiang, T. D. Azad and N. R. Crawfor, "Robotic Spine Surgery: Current State in Minimally Invasive Surgery," *Global Spine Journal,* vol. 10, p. 34S–40S, 2020.

[3] M. D'Souza, J. Gendreau, A. Feng, L. H. Kim, A. L. Ho and A. Veeravagu, "Robotic-Assisted Spine Surgery: History, Efficacy, Cost, And Future Trends," *Robotic Surgery: Research and Reviews,* vol. 6, p. 9–23, 2019.

[4] iData Research, "U.S. Surgical Navigation and Robotics Market," 2024.

[5] F. Avrumova, S. Ahilan, R. K. Alluri, A. Vaishnav, S. Qureshi and D. R. Lebl, "Workflow and Efficiency of Robotic-Assisted Navigation in Spine Surgery," *HSS journal : the musculoskeletal journal of Hospital for Special Surgery,* vol. 17, pp. 302-307, 2021.

[6] Hussain, I., Cosar, M., Kirnaz, S., et al., "Evolving Navigation, Robotics, and Augmented Reality in Minimally Invasive Spine Surgery," *Global Spine Journal,* vol. 10, p. 22S–33S, 2020.

[7] S. V. a. S. Qureshi, "Navigation in minimally invasive spine surgery," *Journal of Spine Surgery,* vol. 5, pp. S25-S30, 2019.

[8] R. Li, A. Davoodi, M. Timmermans, K. Van Assche, O. Taylan, L. Scheys, M. Tummers, G. Borghesan and E. V. Poorten, "Ultrasound-Based Robot-Assisted Drilling for Minimally Invasive Pedicle Screw Placement," *IEEE Transactions on Medical Robotics and Bionics,* vol. VOL. 6, no. NO. 3, August 2024.

[9] A. D. Smith, J. Chapin, P. V. Birinyi, P. V. Bhagvath and A. F. Hall, "Automated Polyaxial Screw Placement Using a Commercial-Robot-Based, Image-Guided Spine Surgery System," *IEEE Transactions on Medical Robotics and Bionics,* vol. VOL. 3, no. NO. 1, February 2021.

[10] M.-C. Kim, E.-S. Kim, J.-O. Park, E. Choi and C.-S. Kim, "Robotic Localization Based on Planar Cable Robot and Hall Sensor Array Applied to Magnetic Capsule Endoscope," *Sensors,* vol. 20, no. 20, 2020.

[11] S. Gervasoni, N. Pedrini, T. Rifai, C. Fischer, F. C. Landers, M. Mattmann, R. Dreyfus, S. Viviani, A. Veciana, E. Masina, B. Aktas, J. Puigmartí-Luis, C. Chautems, S. Pané and Boehler, "A Human-Scale Clinically Ready Electromagnetic Navigation

System for Magnetically Responsive Biomaterials and Medical Devices," *Advanced Materials,* vol. 36, no. 31, 2024.

[12] Northern Digital Inc., "Aurora®," [Online]. Available: https://www.ndigital.com/electromagnetic-tracking-technology/aurora/. [Accessed 20 February 2025].

[13] A. K. Teshome, B. Kibret and D. T. H. Lai, "A Review of Implant Communication Technology in WBAN: Progress and Challenges," *IEEE Reviews In Biomedical Engineering,* vol. 12, 2019.

[14] Qorvo, "Ultra-wideband Technology," [Online]. Available: https://www.qorvo.com/innovation/ultra-wideband/technology. [Accessed 20 February 2025].

[15] Decawave, "DWM1000 IEEE 802.15.4-2011 UWB Transceiver Module - Product Overview," 2016.

[16] G. I. Hapsari, R. Munadi, B. Erfianto and I. D. Irawati, "Accuracy Improvement for Indoor Positioning Using Decawave on ESP32 UWB Pro with Display and Regression," *Journal of Robotics and Control (JRC),* vol. 5, no. 3, p. DOI: 10.18196/jrc.v5i3.20825, 2024.

[17] M. F. R. Al-Okby, S. Junginger, T. Roddelkopf and K. Thurow, "UWB-Based Real-Time Indoor Positioning Systems: A Comprehensive Review," *Applied Sciences,* 11 2024.

[18] A. Poulose and D. S. Han, "UWB Indoor Localization Using Deep Learning LSTM Networks," *Applied Sciences,* vol. 10, no. 18, 2020.